Sensorless Control of Planar Switched Reluctance Motors Based on Voltage Injection Combined With Core-Loss Calculation

Nan Chen ⬤, Guang-Zhong Cao ⬤, *Senior Member, IEEE*, Su-Dan Huang ⬤, *Member, IEEE*, and Jun-Di Sun, *Student Member, IEEE*

Abstract—In this article, a position estimation method is proposed to realize sensorless control of planar switched reluctance motor (PSRM) with core loss. First, a square-wave voltage generated through bipolar pulsewidth modulation (PWM) is injected into the idle phase of a PSRM, thereby generating core loss. The corresponding core-loss average power (CLAP), which contains position information, is calculated in real time. Then, depending on the six-phase CLAP, the initial position can be estimated for the PSRM startup. To stabilize the position estimation in different regions of pole pitches, position data measured in a long stroke are utilized to determine a function mapping from the CLAP with respect to position. Furthermore, a sensorless control system and commutation strategy are designed. Finally, the capability of different methods for position estimation and sensorless control of a PSRM system are experimentally investigated. The feasibility and effectiveness of the proposed method are verified through the experimental results.

Index Terms—Core-Loss calculation, planar switched reluctance motor (PSRM), position estimation, sensorless control, voltage injection.

I. INTRODUCTION

PLANAR direct-drive positioning devices have attracted increased attention because of their simple structure, low friction, and no backlash, which are substantial advantages over conventional planar positioning devices with cumbersome mechanical transmission mechanisms [1]–[3]. A planar switched reluctance motor (PSRM) is a kind of planar direct-drive positioning device. In addition to the merits mentioned above, PSRMs are also low cost, exhibit high reliability without permanent magnet utilization, and provide high heat dissipation for air-contacted stator arrays and phase windings [4], [5].

Rotary switched reluctance motors (RSRMs), linear switched reluctance motors (LSRMs), and PSRMs operate based on the minimum reluctance principle [4]. Hence, position information is crucial for PSRM commutation and position control. Position information is generally detected by position sensors, such as optical encoders or magnetic sensors. However, the utilization of position sensors limits PSRMs by increasing cost, decreasing reliability, increasing system complexity, and introducing electrical connection problems. To overcome such drawbacks, it is imperative to investigate suitable position estimation methods to realize sensorless control of PSRMs.

Over the last few decades, many position estimation methods have been proposed for RSRMs or LSRMs with a wide speed range from standstill to high speeds. Considering the restrictions in stroke and acceleration, operation of PSRMs can be deemed as low speed. Hence, low-speed position estimation methods should be emphasized for PSRMs, and these methods can be mainly classified as pulse injection methods [6]–[8], current waveform methods [9]–[11], flux linkage methods [12], [13], observer-based methods [14]–[17], intelligent methods [18]–[20], and component-addition-based methods [21]–[23].

The flux linkage method is based on the fact that the flux linkage is a function of the phase current and position; however, this method is associated with high memory utilization and high computational costs. For less memory utilization and a simpler computation, an improved flux linkage comparison scheme was proposed in [12]. To improve the measurement accuracy of the flux linkage, an automated resistance correction is adopted for RSRM sensorless control [13]. However, for a PSRM, the magnetic characteristics should be obtained from a two-dimensional (2-D) plane, which is complicated and time-consuming process. For the observer-based method, adaptive state observers [14] and sliding mode observers [15], [16] have been applied to estimate the rotor position for RSRMs. However, the estimation accuracy in this approach is easily affected by model inaccuracies and disturbances. For PSRMs, a sliding mode observer was adopted to

achieve position estimation in [17], but sensorless control was not realized. The intelligent method often combines flux linkage characteristics and uses artificial neural networks [18], fuzzy logic [19], or a combination thereof [20] for position estimation. Although the intelligent method can reduce memory utilization, this method is still inconvenient to implement. The component-addition-based method requires additional components, such as search coils [21], [22] and bootstrap circuits [23]. This method may lead to assembly problems and increased spatial occupation. The current waveform method utilizes the current slope during the chopping period to obtain the inductance characteristics of a switched-reluctance-type motor and subsequently estimate position [9]–[11]. The back electromotive force and resistive voltage drop can be compensated by the current slope difference in the rising region and descending region [24]. The principle of the pulse injection method is similar to that of the current waveform method, but the current waveform used for slope calculation in the former is generated by injecting voltage rather than current chopping [6], [7].

For the traditional pulse injection method and the current waveform method, the calculation of phase inductance is crucial. The variation in the phase inductance of PSRMs is much smaller than that in other switched-reluctance-type motors because PSRMs have a much smaller pole pitch. Thus, phase inductance calculation errors would cause more substantial negative effects in PSRMs than in other switched-reluctance-type motors. Additionally, due to the relatively large core loss generated in PSRMs [25], the phase current caused by an injected voltage is distorted because of the effect of core loss, which leads to significant errors in phase inductance calculation. Hence, such traditional sensorless methods cannot be directly applied to PSRMs without producing unacceptable errors in position estimation.

Although an inductance compensation method considering core loss was proposed in [8], a linear approximation of the current slope was still adopted. In [26], a position estimation method was proposed based on the difference in current rising time caused by the eddy current effect. However, the current rising time needs to be measured accurately, and the precision of position estimation should be improved. Therefore, to apply the pulse injection method for achieving sensorless control in PSRMs considering the effect of core loss, a position estimation method based on voltage injection combined with core-loss calculation is proposed in this article. This method avoids current slope calculation and focuses instead on power calculation. In contrast to the differential operation of the current slope calculation used in traditional methods, the power calculation in the proposed method involves an integral operation that can notably reduce current noise. Moreover, the proposed method needs only one current sensor per phase and does not require a voltage sensor, thereby reducing the system cost further. The main contributions of this article are as follows:

1) proposing a real-time core-loss calculation method;
2) proposing a position estimation method that considers core loss;
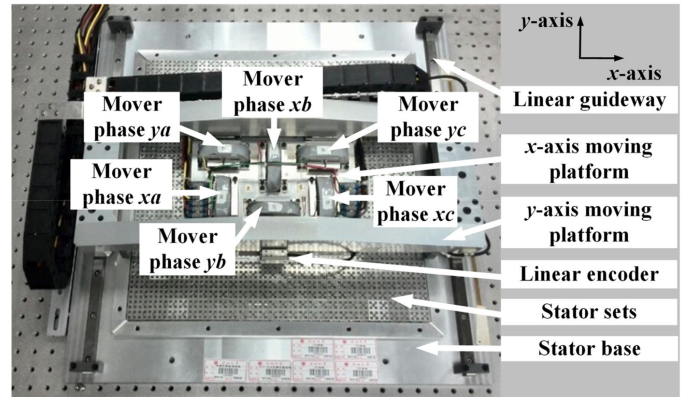3) extending the theories of position estimation and sensorless control to PSRMs;
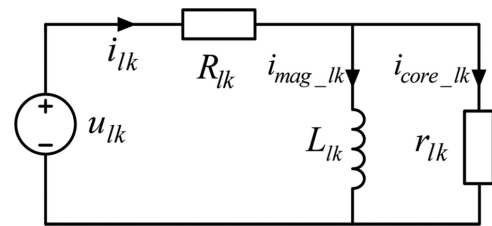

Fig. 1.   Overall structure of the PSRM prototype.

Fig. 2.   Equivalent phase circuit of the PSRM considering core loss.

4) realizing sensorless control of PSRMs for the first time by implementing the proposed methods.

II. DESCRIPTION OF THE PSRM SYSTEM

A. Mechanical Structure

The PSRM prototype developed in our laboratory is presented in Fig. 1, and the specifications of this device are listed in [5]. This PSRM can be regarded as two LSRMs with orthogonal magnetic circuits, consisting of a stator base, stator sets, x- and y-axis moving platforms, x- and y-axis linear guides, and x- and y-axis linear optical encoders. The y-axis moving platform is composed of an x-axis moving platform and a sliding plate. The x-axis moving platform is composed of two sets of three identical movers. These two sets of movers are perpendicular to each other, and each set of movers is responsible for one axial motion. Phases xa, xb, and xc and phases ya, yb, and yc are the three-phase windings in the x- and y-axis, respectively. The stator block and mover are fabricated from a set of laminated silicon steels.

B. Modeling

Since the two sets of three-phase windings in the PSRM are decoupled magnetically [1], the mutual inductances of each winding are negligible, and the electromagnetic forces in the two axes are independently generated with little mutual influence.

The equivalent phase circuit considering core loss is shown in Fig. 2 [27]. For phase k in the l-axis, the voltage balance
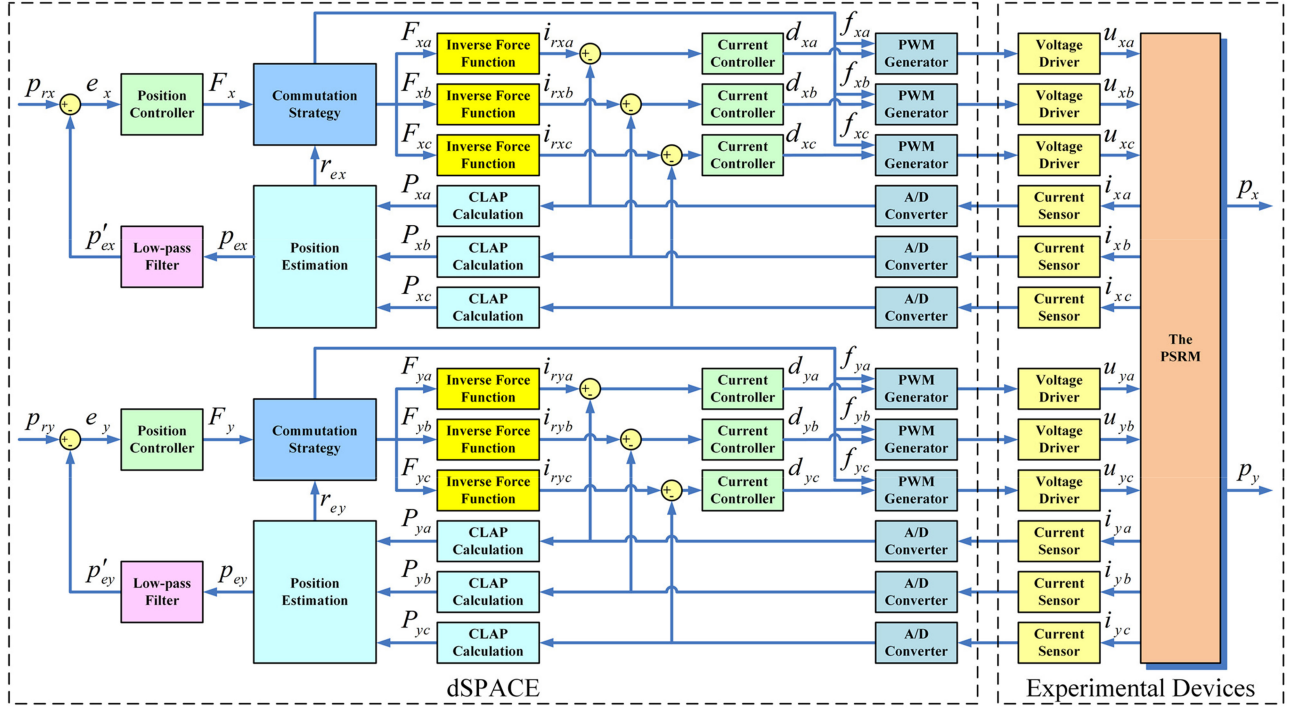
Fig. 3. Block diagram of the PSRM sensorless control system.

equation is given by

$$
\begin{cases}
i_{lk}(t) = i_{\text{mag\_}lk}(t) + i_{\text{core\_}lk}(t) \\
u_{lk}(t) = i_{lk}(t)R_{lk} + \dfrac{d\psi_{lk}\left(i_{\text{mag\_}lk}(t), p_l(t)\right)}{dt} \\
u_{lk}(t) = i_{lk}(t)R_{lk} + i_{\text{core\_}lk}(t)r_{lk}(i_{\text{core\_}lk}(t), p_l(t))
\end{cases}
\tag{1}
$$

where i_{lk}, $i_{\text{mag\_}lk}$, and $i_{\text{iron\_}lk}$ are the phase current, magnetizing current, and core-loss current of phase lk ($l = x$, y; $k = a$, b, c), respectively; p_l is the moving platform position in the l-axis; and u_{lk}, R_{lk}, r_{lk}, and Ψ_{lk} are the voltage, equivalent winding resistance, equivalent incremental core-loss resistance, and flux linkage of phase lk, respectively.

The derivative of the flux linkage can be represented by

$$
\begin{aligned}
\frac{d\psi_{lk}(i_{\text{mag\_}lk}(t), p_l(t))}{dt} &= \frac{\partial\psi_{lk}(i_{\text{mag\_}lk}(t), p_l(t))}{\partial i_{\text{mag\_}lk}(t)}\frac{di_{\text{mag\_}lk}(t)}{dt} \\
&+ \frac{\partial\psi_{lk}(i_{\text{mag\_}lk}(t), p_l(t))}{\partial p_l(t)}\frac{dp_l(t)}{dt} \\
&= e_{\text{ind\_}lk}(t) + e_{\text{mot\_}lk}(t)
\end{aligned}
\tag{2}
$$

where $e_{\text{ind\_}lk}$ is the induced electromotive force and $e_{\text{mot\_}lk}$ is the motional electromotive force.

According to the definition of inductance, the flux linkage can be expressed as

$$
\psi_{lk}(i_{\text{mag\_}lk}(t), p_l(t)) = L_{lk}(i_{\text{mag\_}lk}(t), p_l(t))i_{\text{mag\_}lk}(t)
\tag{3}
$$

where L_{lk} is the inductance of phase lk.

Substituting (3) into (2) yields

$$
\begin{aligned}
e_{\text{ind\_}lk}(t) = &\left(L_{lk}(i_{\text{mag\_}lk}(t), p_l(t)) \right. \\
&\left. + i_{\text{mag\_}lk}(t)\frac{\partial L_{lk}(i_{\text{mag\_}lk}(t), p_l(t))}{\partial i_{\text{mag\_}lk}} \right)\frac{di_{\text{mag\_}lk}(t)}{dt}
\end{aligned}
\tag{4}
$$

$$
e_{\text{mot\_}lk}(t) = i_{\text{mag\_}lk}(t)\frac{\partial L_{lk}(i_{\text{mag\_}lk}(t), p_l(t))}{\partial p_l}v_l(t)
\tag{5}
$$

where v_l is the l-axis speed. In [5], the thrust force is given as

$$
\begin{aligned}
F_l(t) &= \sum_{k=a}^{c} F_{lk}(i_{\text{mag\_}lk}(t), p_l(t)) \\
&= \sum_{k=a}^{c} \frac{\partial \int_0^{i_{\text{mag\_}lk}(t)} \psi_{lk}(I(t), p_l(t))dI(t)}{\partial p_l(t)}
\end{aligned}
\tag{6}
$$

where F_l and F_{lk} are the thrust forces along the l-axis and of the phase lk, respectively.

Since $i_{\text{core\_}lk}$ is much less than $i_{\text{mag\_}lk}$, $i_{\text{mag\_}lk}$ is approximately equal to i_{lk}. Therefore, by replacing $i_{\text{mag\_}lk}$ with i_{lk}, the thrust force under a linear magnetic field can be expressed as [5]

$$
F_l(t) = \sum_{k=a}^{c} \frac{1}{2}\frac{dL_{lk}(p_l(t))}{dp_l(t)}i_{lk}^2(t).
\tag{7}
$$

C. Sensorless Control System

Fig. 3 depicts the block diagram of the PSRM sensorless control system. Two proportional–derivative (PD) position controllers with a 1 kHz control frequency are provided to control

the x- and y-axis positions. Six proportional-integral (PI) current controllers are implemented with a 10 kHz control frequency to control the current of all six phases.

Neglecting friction, the transfer function from thrust force to position can be represented by

$$G_1(s) = \frac{p_l(s)}{F_l(s)} = \frac{1}{M_l s^2 + C_l s} \tag{8}$$

where M_l and C_l are the mass of the moving platform and the damping coefficient in the l-axis, respectively.

For the phase winding, the transfer function from phase voltage to phase current can be expressed as

$$G_2(s) = \frac{i_{lk}(s)}{u_{lk}(s)} = \frac{1}{L_{lk}s + R_{lk}}. \tag{9}$$

To reduce the model complexity, L_{lk} and R_{lk} are set to the average phase inductance and a constant value, respectively.

To determine the parameters of PD and PI controllers, (8) and (9) are imported into the proportional–integral–derivative (PID) Tuner Toolbox in MATLAB, and these parameters are adjusted to ensure that the step responses have no overshoot and that the settling time is as short as possible. Because there are differences between the actual system and the theoretical system, the obtained parameters also need slight adjustment in the actual system. Finally, the parameters of the PD and PI controllers are determined.

Six current sensors are utilized to detect the phase current for current control and core-loss average power (CLAP) calculation. Six voltage drivers with H-bridges are adopted to power the six-phase winding and to generate square waves for voltage injection via bipolar pulsewidth modulation (PWM).

The inverse force function is introduced to calculate the phase current command according to the phase thrust force command. In terms of (7), the inverse force function of phase lk is represented by

$$i_{rlk}(t) = \sqrt{2F_{lk}(t)\left(\frac{dL_{lk}(p_l(t))}{dp_l(t)}\right)^{-1}} \tag{10}$$

where i_{rlk} is the phase current command of phase lk.

According to (10), i_{rlk} is related to the derivative of the inductance with respect to position, which goes against sensorless control and increases complexity. Hence, a positive constant slope G is used to represent the slope of the inductance-position curve in a monotonous area. The inverse force function can be given as

$$i_{rlk}(t) = \sqrt{2F_{lk}(t)G^{-1}}. \tag{11}$$

According to the actual inductance-position curve of the PSRM, G is determined as 1.11 mH/mm.

The operating principles of the x-axis motion and y-axis motion are similar. For x-axis linear motion, the actual position p_x is estimated as p_{ex} by the sensorless position estimation method. The position r_{ex} in a pole pitch ranges from 0 to τ mm, where τ is the pole pitch of the mover and stator, and this position is used for the commutation of the PSRM. A moving average low-pass filter with a span of 15 points is employed to filter

TABLE I
COMMUTATION STRATEGY IN ONE AXIS

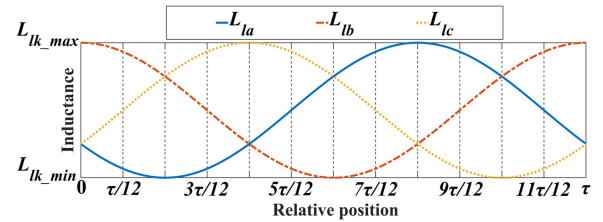| Thrust force command	Position in a pole pitch	Conducted phase	Injected phase
$F_l > 0$	$[11\tau/12, \tau) \cup [0, 3\tau/12)$	c	a, b
$F_l > 0$	$[3\tau/12, 7\tau/12)$	a	b, c
$F_l > 0$	$[7\tau/12, 11\tau/12)$	b	a, c
$F_l < 0$	$(9\tau/12, \tau) \cup [0, \tau/12]$	a	b, c
$F_l < 0$	$(5\tau/12, 9\tau/12]$	c	a, b
$F_l < 0$	$(\tau/12, 5\tau/12]$	b	a, c

Fig. 4. Three-phase inductance curves in the l-axis.

out noise from the estimated position p_{ex}, providing a position feedback signal p'_{ex} to the position control. The position error e_x is generated by comparing p'_{ex} and the reference position p_{rx}, and is processed with the x-axis position controller to produce the x-axis thrust force command F_x. In terms of F_x and r_{ex}, the three-phase thrust force commands F_{xa}, F_{xb}, and F_{xc} are generated by the commutation strategy. Through the inverse force functions, three-phase current commands i_{rxa}, i_{rxb}, and i_{rxc} are obtained. The actual three-phase currents i_{xa}, i_{xb}, and i_{xc} are measured with current sensors, and these measurements are fed back to the current controllers for generating duty cycles for the PWM generators. The three x-axis voltage drivers output the proper voltages to the PSRM according to the PWM signal, achieving x-axis linear motion.

D. Commutation Strategy

The commutation strategy is shown in Table I. The following can be concluded from Table I.
1) The commutation is dependent on both the direction of the thrust force command and the position in a pole pitch.
2) When the direction of the thrust force command is changed, the commutation region of each phase is correspondingly changed.
3) The commutation region per phase is $\tau/3$.
4) For the motion in one axis of the PSRM, all three phases are fully employed, of which one phase is used as the conducted phase and the other two phases are applied as the injected phase.

The three-phase inductance curves in the l-axis are shown in Fig. 4. A phase will be conducted when it has a positive inductance slope in the motion direction. Once the phase is no longer conducted, it becomes an idle phase. When the phase

current of the idle phase decreases to zero, the injection will start immediately.

The voltage injection is achieved by changing only the frequency of the PWM signal, which can be conveniently achieved in the actual system. When a phase is conducted, the PWM frequency of this phase is set to 50 kHz, and enters the current control mode. When the injection conditions of a phase are satisfied, the PWM frequency of this phase is changed to 500 Hz, and enters the voltage injection mode.

III. CORE-LOSS CALCULATION

A. Core Loss

The core loss in a switched-reluctance-type motor is dependent on many factors, including the magnetic material characteristics, operating frequency, and flux density. However, the magnetic material characteristics are fixed for a specific PSRM. And for an injected phase, if the amplitude and frequency of the injected square-wave voltage are fixed, the flux and operating frequency are distinct. Nevertheless, although the flux is fixed, the distribution of the flux density is still affected by the position, indicating that core loss is related to the position. Thus, only the relationship between the core loss and position should be considered for a specific PSRM.

For RSRM, the equivalent incremental core-loss resistance r_{lk} is related to the rotor position, and the value of r_{lk} at the aligned position is less than that at the fully unaligned position [27], [28]. Similarly, the position information of the PSRM is also reflected by r_{lk}. However, because it is difficult to obtain r_{lk} directly in the actual system, a power-calculation-based method is considered. If the phase current is small, the voltage drop in R_{lk} is negligible compared to the phase voltage. According to (1), the core-loss power $P_{\text{core\_}lk}$ can be expressed as

$$P_{\text{core\_}lk}(t) = \frac{u_{lk}^2(t)}{r_{lk}(t)}. \qquad (12)$$

According to (12), the position information of the PSRM is also contained in $P_{\text{core\_}lk}$. When u_{lk} remains constant, the value of $P_{\text{core\_}lk}$ at the aligned position is larger than that at the fully unaligned position. Therefore, $P_{\text{core\_}lk}$ is a periodic function of the position, and the period of the function is the pole pitch.

B. Proposed CLAP Calculation Method

The injected voltage is a square wave generated through bipolar PWM. For most inverters, because the on-state resistance is much less than the equivalent winding resistance, the resistive voltage drop in the inverter is negligible. Under this condition, the maximum value of the square wave is a positive dc-link voltage U_{dc}, and the minimum value is $-U_{\text{dc}}$. By defining the period of a square wave as T, the total energy consumption $W_{\text{total\_}lk}$ of phase *lk* in one square-wave period can be expressed as

$$W_{\text{total\_}lk} = \int_{t_0}^{t_0+T} u_{lk}(t)i_{lk}(t)dt. \qquad (13)$$

According to (4), because the average power of the inductor in one period is zero, the energy consumption of the inductor

$W_{\text{ind\_}lk}$ is represented by

$$W_{\text{ind\_}lk} = \int_{t_0}^{t_0+T} e_{\text{ind\_}lk}(t)i_{\text{mag\_}lk}(t)dt. \qquad (14)$$

The mechanical energy $W_{\text{mec\_}lk}$ in one square-wave period can be expressed as

$$
\begin{aligned}
W_{\text{mec\_}lk} &= \int_{t_0}^{t_0+T} e_{\text{mot\_}lk}(t)i_{\text{mag\_}lk}(t)dt \\
&= \int_{t_0}^{t_0+T} \frac{\partial L_{lk}(i_{\text{mag\_}lk}(t), p_l(t))}{\partial p_l} v_l(t)i_{\text{mag\_}lk}^2(t)dt.
\end{aligned} \qquad (15)
$$

Due to the limited stroke and acceleration of the PSRM, the speed cannot be accelerated to a large value. Furthermore, when a phase is in the voltage injection mode, the phase current caused by the injected voltage is obviously smaller than the conducting current. According to (15) and assuming that the PSRM operates at a low speed, $W_{\text{mec\_}lk}$ is approximately zero.

According to (1), the copper loss $W_{\text{cop\_}lk}$ can be calculated as

$$W_{\text{cop\_}lk} = \int_{t_0}^{t_0+T} i_{lk}^2(t)R_{lk}dt. \qquad (16)$$

An analysis of the components of the total energy consumption shows that $W_{\text{total\_}lk}$ can also be expressed as

$$W_{\text{total\_}lk} = W_{\text{ind\_}lk} + W_{\text{mec\_}lk} + W_{\text{cop\_}lk} + W_{\text{core\_}lk} \qquad (17)$$

where $W_{\text{core\_}lk}$ is the core loss.

To calculate $W_{\text{core\_}lk}$, (13)–(16) can be substituted into (17), which yields

$$
\begin{aligned}
W_{\text{core\_}lk} &= W_{\text{total\_}lk} - W_{\text{cop\_}lk} \\
&= \int_{t_0}^{t_0+T} u_{lk}(t)i_{lk}(t)dt - \int_{t_0}^{t_0+T} i_{lk}^2(t)R_{lk}dt \\
&= \int_{t_0}^{t_0+T} (u_{lk}(t) - i_{lk}(t)R_{lk})i_{lk}(t)dt. \qquad (18)
\end{aligned}
$$

Hence

$$P_{lk} = \frac{W_{\text{core\_}lk}}{T} = \frac{\int_{t_0}^{t_0+T}(u_{lk}(t) - i_{lk}(t)R_{lk})i_{lk}(t)dt}{T} \qquad (19)$$

where P_{lk} is the CLAP in one period.

To calculate P_{lk} in real time, a PWM rising-edge triggered analog-to-digital converter (ADC) burst sampling technique is employed to sample the phase current. By setting the number of burst sampling points as M, P_{lk} can be calculated in real time by

$$P_{lk} = ((\boldsymbol{U}_{M\times1} - \boldsymbol{I}_{M\times1}R_{1\times1})\boldsymbol{I}_{M\times1})^T \boldsymbol{\Delta T}_{M\times1}T_{1\times1}^{-1} \qquad (20)$$

where $\boldsymbol{I}_{M\times1}$ and $R_{1\times1}$ are the phase current sample vector and the equivalent winding resistance, respectively, and $\boldsymbol{\Delta T}_{M\times1}$ is the time interval vector, which is expressed as

$$\boldsymbol{\Delta T}_{M\times1} = [\Delta t, \Delta t, \dots, \Delta t]^T, \Delta t = \frac{T}{M} \qquad (21)$$

where Δt is the ADC burst sampling interval.

The phase voltage vector is

$$U_{M \times 1} = \left[u_1, u_2, \ldots, u_{M/2}, u_{M/2+1}, u_{M/2+2}, \ldots, u_M \right]^T$$

$$u_j = \begin{cases} U_{\mathrm{dc}}, & j \in [1, M/2] \cap N^* \\ -U_{\mathrm{dc}}, & j \in [M/2+1, M] \cap N^* \end{cases}. \qquad (22)$$

Because the dc-link voltage U_{dc} is known, there is no requirement for a voltage sensor.

IV. PROPOSED POSITION ESTIMATION METHOD

A. Initial Position Estimation Method

The initial position is crucial for the PSRM startup from a standstill. The initial position can be obtained by injecting voltage to all phases and calculating the corresponding CLAP.

The mapping from the l-axis position p_l to CLAP P_{lk} of phase lk is a periodic function, which can be expressed as a Fourier series

$$P_{lk} = f_{lk}(p_l) = P_{lk0} + \sum_{n=1}^{\infty} P_{lkn} \sin\left(n\omega p_l + \varphi_{lkn} \right) \qquad (23)$$

where f_{lk} is the function mapping, n is a positive integer, ω is the angular frequency of the first harmonic, P_{lk0} is the dc component, P_{lkn} is the amplitude of the nth harmonic, and φ_{lkn} is the initial phase angle of the nth harmonic.

The angular frequency of the first harmonic is expressed as

$$\omega = \frac{2\pi}{\tau}. \qquad (24)$$

According to the mechanical structure of the PSRM, the relative angles between the three-phase movers in the l-axis are $2\pi/3$ radians. By neglecting the harmonics where $n > 1$ and assuming that the position of $p_l = 0$ is the aligned position of phase lb, the l-axis three-phase CLAP is given as

$$\begin{cases} P_{la} = P_{la0} + P_{la1} \cos\left(\dfrac{2\pi}{\tau} p_l + \dfrac{2\pi}{3} \right) \\[2mm] P_{lb} = P_{lb0} + P_{lb1} \cos\left(\dfrac{2\pi}{\tau} p_l \right) \\[2mm] P_{lc} = P_{lc0} + P_{lc1} \cos\left(\dfrac{2\pi}{\tau} p_l - \dfrac{2\pi}{3} \right) \end{cases}. \qquad (25)$$

Defining the a-, b-, and c-axis with a relative angle of $2\pi/3$ radians and the orthogonal α- and β-axis, let the α-axis coincides with the b-axis, as shown in Fig. 5. P_{la}, P_{lb}, and P_{lc} are defined as 1-D vectors along the a-, b-, and c-axis, respectively, where P_l is the vector sum of P_{la}, P_{lb}, and P_{lc}. P_l is then projected to the orthogonal α- and β-axis, obtaining $P_{l\alpha}$ and $P_{l\beta}$, respectively. Therefore, a transformation from P_{la}, P_{lb}, and P_{lc} to $P_{l\alpha}$ and $P_{l\beta}$ can be expressed as

$$\begin{bmatrix} P_{l\alpha} \\ P_{l\beta} \end{bmatrix} = \begin{bmatrix} -\dfrac{1}{2} & 1 & -\dfrac{1}{2} \\[2mm] -\dfrac{\sqrt{3}}{2} & 0 & \dfrac{\sqrt{3}}{2} \end{bmatrix} \begin{bmatrix} P_{la} \\ P_{lb} \\ P_{lc} \end{bmatrix}. \qquad (26)$$
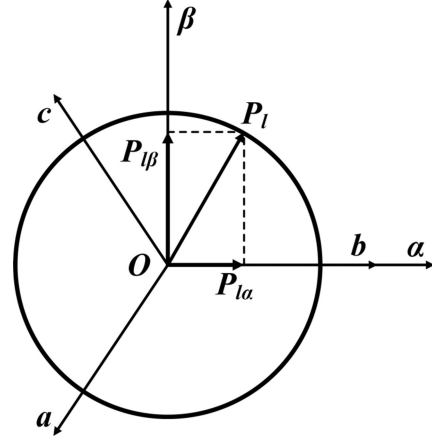

Fig. 5. Coordinate systems a–b–c and α–β.

Substituting (25) into (26) and assuming that $P_{la0} = P_{lb0} = P_{lc0}$ and $P_{la1} = P_{lb2} = P_{lc3} = P_{l1}$ yields

$$\begin{bmatrix} P_{l\alpha} \\ P_{l\beta} \end{bmatrix} = \begin{bmatrix} \dfrac{3}{2} P_{l1} \cos\left(\dfrac{2\pi}{\tau} p_l \right) \\[3mm] \dfrac{3}{2} P_{l1} \sin\left(\dfrac{2\pi}{\tau} p_l \right) \end{bmatrix}. \qquad (27)$$

Hence, the estimated initial position $p_{\mathrm{init\_est\_}l}$ of the l-axis can be expressed as

$$p_{\mathrm{init\_est\_}l} = \frac{\tau}{2\pi} \arctan\left(\frac{P_{l\beta}}{P_{l\alpha}} \right). \qquad (28)$$

Considering the signs of $P_{l\beta}$ and $P_{l\alpha}$, the full-range of $p_{\mathrm{init\_est\_}l}$ can be obtained, which is $[0, \tau)$.

B. Position Estimation Method for a Long Stroke

According to (23), if the function mapping f_{lk} is obtained accurately, the l-axis estimated position $p_{\mathrm{est\_}l}$ can be obtained by

$$p_l = f_{lk}^{-1}(P_{lk}). \qquad (29)$$

Because f_{lk} is a periodic function, the traditional method utilizes the function fitting to determine f_{lk}^{-1} based on monotonic interval data in a short stroke [8], [26], [29]. A short stroke is a relative concept corresponding to a long stroke, which consists of many pole pitches. For a PSRM, because of the large number of pole pairs, existing manufacture tolerances [30], and the different core-loss conditions under different pole pitches, monotonic interval data in a short stroke cannot sufficiently reflect the function relation in a long stroke without resulting in significant fitting errors.

For the purpose of overcoming this drawback, a position fitting method is proposed for a long stroke. Since the relative angles between the three-phase movers in the l-axis are $2\pi/3$ radians, the positions of the three-phase movers in the l-axis can be transformed from the moving platform position p_l to periodic
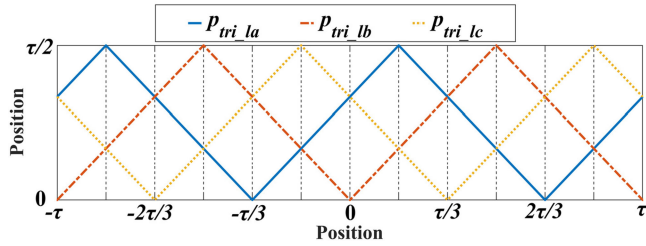
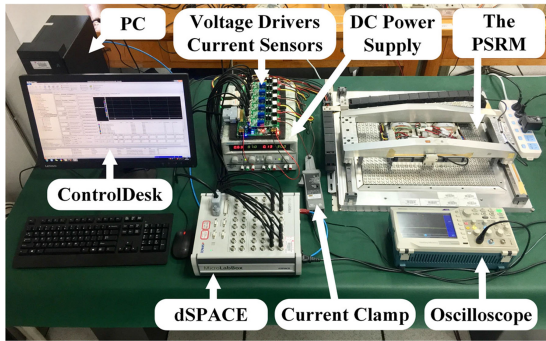Fig. 6. Three-phase position triangular wave in the *l*-axis.

Fig. 8. Phase current caused by injected a bipolar square-wave voltage.

Fig. 7. Experimental setup of the PSRM system.

Fig. 9. CLAP versus position. (a) *x*-axis CLAP. (b) *y*-axis CLAP.

three-phase position triangular waves by

$$
\begin{cases}
p_{\text{tri\_}la} = \frac{\tau}{2\pi}\arccos\left(\cos\left(\frac{2\pi}{\tau}p_l + \frac{2\pi}{3}\right)\right) \\
p_{\text{tri\_}lb} = \frac{\tau}{2\pi}\arccos\left(\cos\left(\frac{2\pi}{\tau}p_l\right)\right) \\
p_{\text{tri\_}lc} = \frac{\tau}{2\pi}\arccos\left(\cos\left(\frac{2\pi}{\tau}p_l - \frac{2\pi}{3}\right)\right)
\end{cases}
\tag{30}
$$

where $p_{\text{tri\_}la}$, $p_{\text{tri\_}lb}$, and $p_{\text{tri\_}lc}$ are the position triangular waves of phases *a*, *b*, and *c* in the *l*-axis, respectively. The transformed results within two pole pitches are shown in Fig. 6. Hence, a new function relation that needs to be fitted is represented by

$$
p_{\text{tri\_}lk} = g_{lk}(P_{lk})
\tag{31}
$$

where g_{lk} is the function mapping from P_{lk} to $p_{\text{tri\_}lk}$.

Since both P_{lk} and $p_{\text{tri\_}lk}$ are periodic functions, the data can be measured from the position of a long stroke of the PSRM, which means that g_{lk} can provide the position information within a long stroke.

To determine g_{lk}, a polynomial fitting is carried out by the least squares method. Considering the fitting precision and calculation complexity, a three-order polynomial is adopted, which is given as

$$
y = a_n x^n + a_{n-1} x^{n-1} + \cdots + a_1 x + a_0, n = 3
\tag{32}
$$

where x, y, a_n, and n are the input, output, coefficient, and order of the polynomial, respectively.

V. EXPERIMENTAL VERIFICATION

A. Experimental Setup

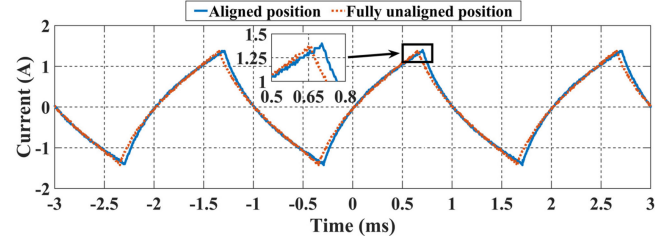Fig. 7 shows the experimental setup of the PSRM system. Six LEM CKSR 6-NP current sensors are employed to measure the

phase current. Six voltage drivers with H-bridges are designed based on TI CSD18533Q5A MOSFETs to power the phase windings. A dc power supply provides a dc-link voltage of 30 V. Two Renishaw TD0400A40A linear optical encoders are used to detect the actual positions of both axes for error analysis. The control software is designed in MATLAB-Simulink, and this software can be seamlessly uploaded to the dSPACE MicroLab-Box to realize real-time control. The graphical user interface is created using ControlDesk and combined with dSPACE for parameter setting and data acquisition.

B. CLAP Calculation

The CLAP calculation is based on the phase current caused by injection, and the typical phase current waveforms of phase *xb* are shown in Fig. 8. The frequency of the injected bipolar PWM voltage is 500 Hz, and R_{xb} is 0.56 Ω. If the core loss is nonexistent, the peak of the phase current should be less at the aligned position than that at the fully unaligned position due to the inductance characteristics. However, the peaks of the phase currents at the two positions are approximately equal. The additional current generated by core loss is most obvious at the aligned position.

The calculated three-phase CLAP of *x*- and *y*-axis are shown in Fig. 9(a) and (b), respectively. Fluctuations in the amplitude
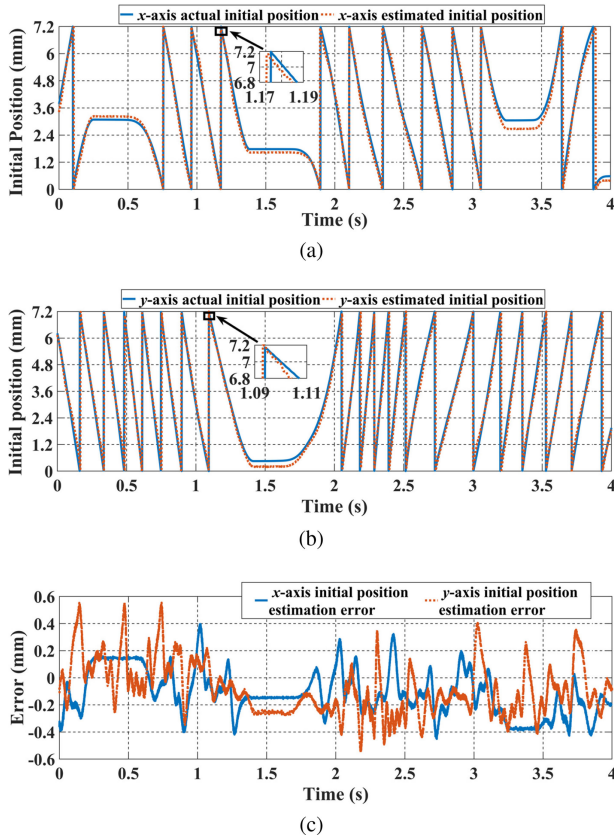
Fig. 10.   Experimental results of the initial position estimation. (a) *x*-axis position. (b) *y*-axis position. (c) *x*- and *y*-axis errors.
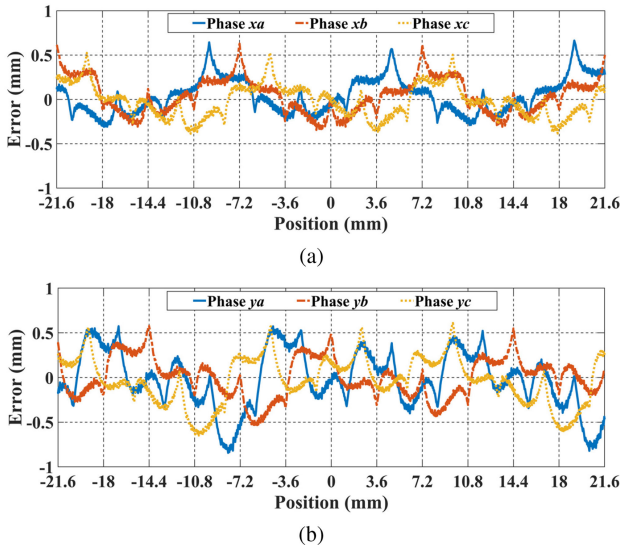

Fig. 11.   Polynomial fitting errors. (a) *x*-axis errors. (b) *y*-axis errors.

are caused by the gaps in the stator array structure. According to the abovementioned theoretical analysis, the CLAP periodically varies with the position, and the period is the pole pitch τ of 7.2 mm. When the phase is aligned, the CLAP increases to a maximum value; when the phase is fully unaligned, the CLAP decreases to a minimum value.
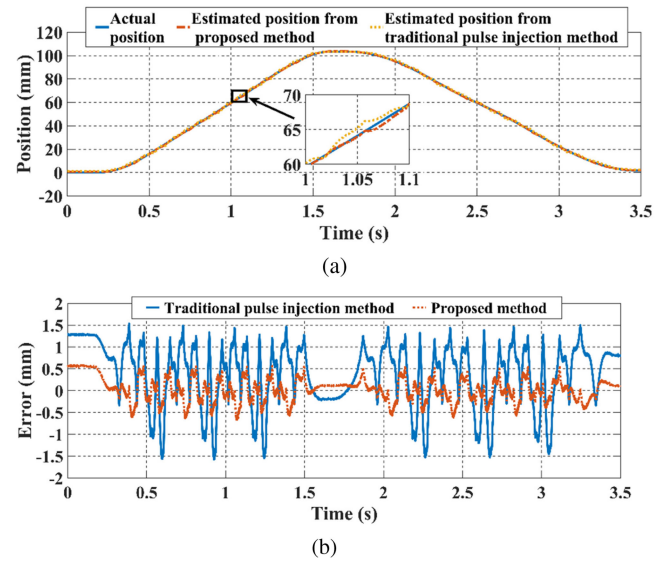

Fig. 12.   Performance comparison of the *y*-axis position estimation under different methods. (a) Actual and estimated positions. (b) Errors in position estimation.

TABLE II
ERRORS IN *y*-AXIS POSITION ESTIMATION UNDER DIFFERENT METHODS

Method	Error type	Value (mm)
Observer-based method	MAE	2.535
	AAE	1.093
Traditional pulse injection method	MAE	1.533
	AAE	0.383
Proposed method	MAE	0.605
	AAE	0.026

TABLE III
PARAMETERS OF THE POSITION AND CURRENT CONTROLLERS

Controller	Parameter	Value
PD *x*-axis position controller	k_{px}	6
	k_{dx}	0.16
PD *y*-axis position controller	k_{py}	10
	k_{dy}	0.22
PI current controller for the six phases	k_p	10.75
	k_i	772.6

C. Initial Position Estimation

Although the initial position estimation should be performed at a standstill, to improve the efficiency of the experiment, the data are acquired when the moving platforms are slowly moved by hand. The performance of the proposed method under low-speed conditions is theoretically worse than that under standstill conditions because of the negligible mechanical energy of the injected phase. Hence, the experimental results for both axes are conservative, which are shown in Fig. 10.

Because the pole pitch τ is 7.2 mm, the position range of $p_{\text{init\_est\_}l}$ is [0, 7.2) mm. After reaching a value of 7.2 mm,

TABLE IV
ERRORS IN POSITION ESTIMATION AND TRAJECTORY TRACKING

Reference trajectory			*x*-axis position estimation (mm)		*y*-axis position estimation (mm)		*x*-axis trajectory tracking (mm)		*y*-axis trajectory tracking (mm)	
Radius (mm)	Period (s)	Velocity (mm/s)	MAE	AAE	MAE	AAE	MAE	AAE	MAE	AAE
30	5	37.70	0.997	0.199	0.900	0.219	1.485	0.440	1.200	0.379
20	3	41.89	0.895	0.199	1.183	0.243	1.281	0.418	1.325	0.353
30	4	47.12	1.213	0.267	1.107	0.199	1.401	0.442	1.401	0.333
30	3	62.83	1.107	0.258	1.204	0.249	1.149	0.348	1.259	0.350
30	2.5	75.40	1.468	0.287	1.527	0.278	1.385	0.321	1.060	0.335
40	3	83.78	1.289	0.268	1.387	0.385	1.085	0.323	0.953	0.415

TABLE V
NORMALIZED ERRORS IN POSITION ESTIMATION AND TRAJECTORY TRACKING

Reference trajectory			*x*-axis position estimation (normalized)		*y*-axis position estimation (normalized)		*x*-axis trajectory tracking (normalized)		*y*-axis trajectory tracking (normalized)	
Radius (mm)	Period (s)	Velocity (mm/s)	MAE	AAE	MAE	AAE	MAE	AAE	MAE	AAE
30	5	37.70	0.679	0.693	0.589	0.569	1.000	0.995	0.857	0.913
20	3	41.89	0.610	0.693	0.775	0.631	0.863	0.946	0.946	0.851
30	4	47.12	0.826	0.930	0.725	0.517	0.943	1.000	1.000	0.802
30	3	62.83	0.754	0.899	0.788	0.647	0.774	0.787	0.899	0.843
30	2.5	75.40	1.000	1.000	1.000	0.722	0.933	0.726	0.757	0.807
40	3	83.78	0.878	0.934	0.908	1.000	0.731	0.731	0.680	1.000

$p_{\text{init\_est\_}l}$ will step to 0 mm. In Fig. 10(a) and (b), positive slope indicates positive movement, whereas negative slope indicates negative movement. In each pole pitch, the estimated initial position is able to track the actual initial position for both axes. The initial position estimation error curves are shown in Fig. 10(c). The *x*-axis error is less than 0.451 mm, and the *y*-axis error is less than 0.555 mm, which demonstrates the effectiveness of the proposed method.

D. Position Estimation for a Long Stroke

The position detected by the linear optical encoder is regarded as the actual position; hence, the position estimation error can be defined as the estimated position minus the actual position. The data for polynomial fitting are sampled from a range that is larger than 200 mm from both the *x*- and *y*-axis. The input sample set is the CLAP of phase *lk*, which is similar to Fig. 9. The output sample set is the position triangular wave of phase *lk,* as shown in Fig. 6. The fitting errors for the *x*- and *y*-axis with a range from −20 to 20 mm are depicted in Fig. 11(a) and (b), respectively. The fitting error for the *x*-axis is less than 0.664 mm, whereas that for the *y*-axis is less than 0.844 mm. The errors are distributed uniformly over the different pole pitches, which establishe the basis for the stability and consistency of the position estimation.

To further verify the superiority of the proposed position estimation method, comparative experiments are carried out utilizing the observer-based method, the traditional pulse injection method, and the proposed method.

The observer-based method was implemented to achieve position estimation of a PSRM in [17], where the maximum absolute error (MAE) and average absolute error (AAE) of

the *y*-axis position estimation were 2.535 and 1.093 mm, respectively. The traditional pulse injection method has not been previously applied to a PSRM, and the core principle of this method is the calculation of phase inductance. Hence, the current-slope-difference method from [24] is adopted in this article to calculate the phase inductance. The *y*-axis position estimation experiment is performed under the condition that the PSRM operates based on close-loop control with a position sensor. The comparative experiment results are shown in Fig. 12 and Table II. For the traditional pulse injection method, the MAE and AAE in position estimation are 1.533 and 0.383 mm, respectively. For the proposed method, the MAE and AAE in position estimation are 0.605 mm and 0.026 mm, respectively. These comparative experiment results verify the superiority of the proposed position estimation method.

For the traditional pulse injection method, the MAEs in position estimation are relatively large compared with the conducting region of a phase. According to the experiment, applying the traditional pulse injection method to the PSRM leads to commutation failure, indicating that this method cannot achieve closed-loop sensorless motion. The observer-based method also causes the same problem. Therefore, such methods were applied to the PSRM system only to perform position estimation experiments.

E. Sensorless Control

Experiments on sensorless control are carried out with a group of circular reference trajectories, which means that two-axis reference positions p_{rx} and p_{ry} are sinusoidal signals with a phase difference of $\pi/2$ radians. By changing the radius and period of the circular reference trajectories, six experiments are
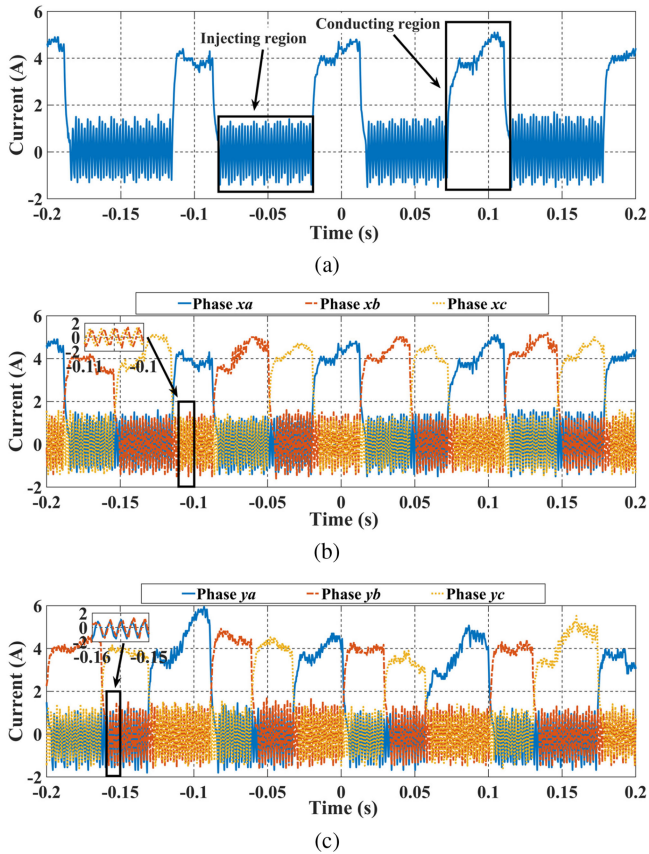
Fig. 13. Phase currents. (a) Current of phase *xa*. (b) Three-phase currents in the *x*-axis. (c) Three-phase currents in the *y*-axis.
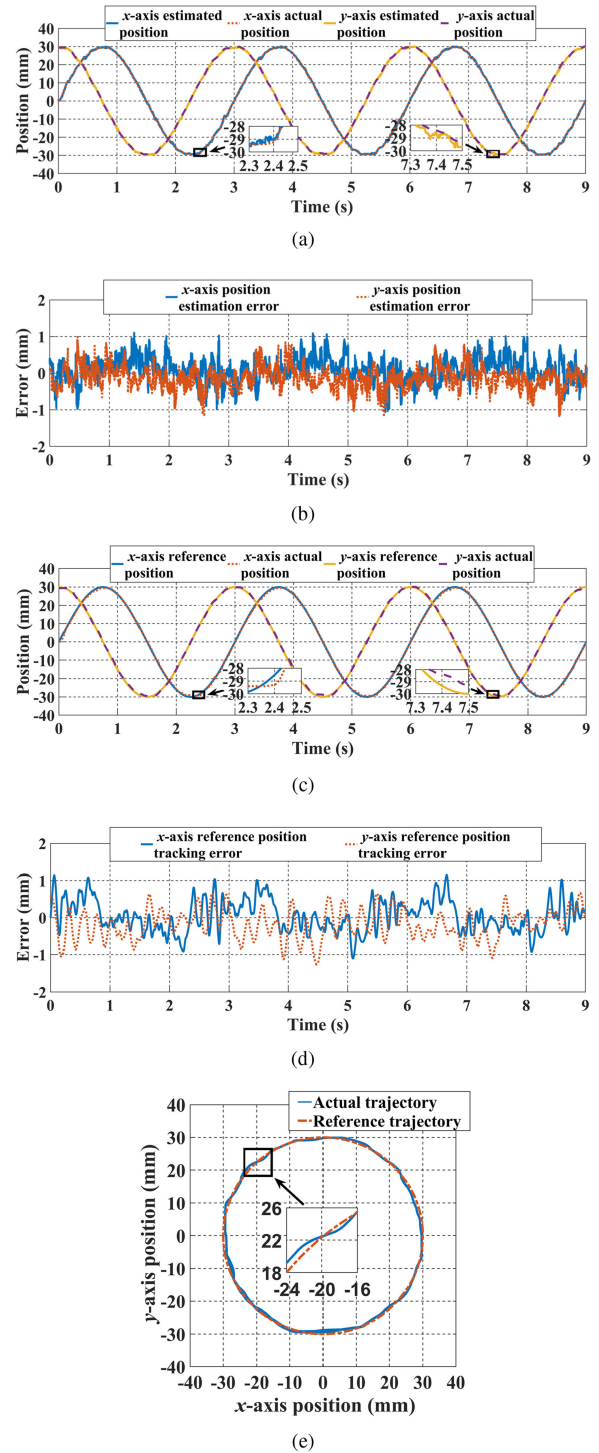

Fig. 14. Experimental results of trajectory tracking. (a) Estimated position. (b) Position estimation errors. (c) Trajectory tracking response. (d) Position tracking errors. (e) 2-D planar trajectory.

implemented. The determined parameters of the position and current controllers listed in Table III are used for the six experiments. The errors in the six experiments are listed in Table IV, and their normalized forms are listed in Table V. The velocity of the reference trajectory is defined as the perimeter divided by the period. Table IV shows that when the PSRM operates under sensorless control, the MAE and AAE of the position estimation for both axes are less than 1.527 and 0.385 mm, respectively, whereas the MAE and the AAE of the trajectory tracking for both axes are less than 1.485 and 0.442 mm, respectively. The normalized AAEs in the position estimation of both axes listed in Table V exhibit an increasing trend as the velocity of the reference trajectory increases. This phenomenon occurs because the mechanical energy in one square-wave period is neglected. Hence, a higher velocity leads to greater errors when calculating the CLAP.

The fifth experiment was carried out through a circular reference trajectory with a radius of 30 mm and a period of 3 s. The corresponding results are depicted in Figs. 13 and 14. Fig. 13(a) presents the current of phase *xa* under the injecting region and conducting region. Fig. 13(b) and (c) show the three-phase current waveforms of both *x*- and *y*-axis. When the PSRM operates, the current control mode and voltage injection mode alternate. Fig. 14(a) shows that the estimated position can dynamically

reflect the actual position detected by the encoder for both axes when the PSRM operates under sensorless closed-loop position control. The position estimation errors in both axes under sensorless control conditions are less than 1.204 mm, as shown in Fig. 14(b). Fig. 14(c) depicts the reference position

and actual position versus time, showing that the actual position can accurately track the reference position. The corresponding tracking errors for both axes are less than 1.259 mm, as shown in Fig. 14(d). Moreover, the circular reference trajectory and two-axis actual trajectories are shown in Fig. 14(e), intuitively demonstrating the tracking performance of the sensorless PSRM control system.

The experimental results indicate that the proposed position estimation method can realize stable two-axis sensorless control of a PSRM system under different reference trajectory conditions.

VI. CONCLUSION

In this article, a position estimation method based on voltage injection combined with core-loss calculation was proposed for PSRMs. The position estimation and sensorless control were analysed experimentally. The experimental results showed that the x- and y-axis errors in the initial position estimation were less than 0.451 and 0.555 mm, respectively; the maximum MAE and AAE in position estimation under sensorless control were 1.527 and 0.385 mm, respectively; and the maximum MAE and AAE in trajectory tracking under sensorless control were 1.485 and 0.442 mm, respectively.

The following conclusions can be drawn.
1) The CLAP can be calculated in real time with the proposed method.
2) The initial position estimation method is capable of estimating the initial position at a standstill.
3) Sensorless control of the PSRM system can be realized in a long stroke based on the stable position estimation.

The feasibility and effectiveness of the proposed method was verified experimentally. This method can also be applied to other similar types of motors, such as RSRMs and LSRMs, as long as a relatively large core loss exists.

REFERENCES

[1] M.-Y. Chen, H.-H. Huang, and S.-K. Hung, "A new design of a submi-cropositioner utilizing electromagnetic actuators and flexure mechanism," *IEEE Trans. Ind. Electron.*, vol. 57, no. 1, pp. 96–106, Jan. 2010.

[2] J. M. M. Rovers, J. W. Jansen, J. C. Compter, and E. A. Lomonova, "Analysis method of the dynamic force and torque distribution in the magnet array of a commutated magnetically levitated planar actuator," *IEEE Trans. Ind. Electron.*, vol. 59, no. 5, pp. 2157–2166, May 2012.

[3] J. W. Jansen, J. P. C. Smeets, T. T. Overboom, J. M. M. Rovers, and E. A. Lomonova, "Overview of analytical models for the design of linear and planar motors," *IEEE Trans. Magn.*, vol. 50, no. 11, Nov. 2014, Art. no. 8206207.

[4] S.-D. Huang, G.-Z. Cao, Z.-Y. He, J. F. Pan, J.-A. Duan, and Q.-Q. Qian, "Nonlinear modeling of the inverse force function for the planar switched reluctance motor using sparse least squares support vector machines," *IEEE Trans. Ind. Informat.*, vol. 11, no. 3, pp. 591–600, Jun. 2015.

[5] S.-D. Huang *et al.*, "Maximum-force-per-ampere strategy of current distribution for efficiency improvement in planar switched reluctance motors," *IEEE Trans. Ind. Electron.*, vol. 63, no. 3, pp. 1665–1675, Mar. 2016.

[6] E. Ofori, T. Husain, Y. Sozer, and I. Husain, "A pulse-injection-based sensorless position estimation method for a switched reluctance machine over a wide speed range," *IEEE Trans. Ind. Appl.*, vol. 51, no. 5, pp. 3867–3876, Sep./Oct. 2015.

[7] K. W. Hu, Y.-Y. Chen, and C.-M. Liaw, "A reversible position sensor-less controlled switched-reluctance motor drive with adaptive and intuitive commutation tunings," *IEEE Trans. Power Electron.*, vol. 30, no. 7, pp. 3781–3793, Jul. 2015.

[8] Q.-L. Wang *et al.*, "Inductance estimation method for linear switched reluctance machines considering iron losses," *IET Electr. Power Appl.*, vol. 10, no. 3, pp. 181–188, Mar. 2016.

[9] B. Fahimi, A. Emadi, and R. B. Sepe, "Four-quadrant position sensorless control in SRM drives over the entire speed range," *IEEE Trans. Power Electron.*, vol. 20, no. 1, pp. 154–163, Jan. 2005.

[10] P. P. Acarnley, R. J. Hill, and C. W. Hooper, "Detection of rotor position in stepping and switched motors by monitoring of current waveforms," *IEEE Trans. Ind. Electron.*, vol. IE-32, no. 3, pp. 215–222, Aug. 1985.

[11] J. Ye, B. Bilgin, and A. Emadi, "Elimination of mutual flux effect on rotor position estimation of switched reluctance motor drives," *IEEE Trans. Power Electron.*, vol. 30, no. 3, pp. 1499–1512, Mar. 2015.

[12] I. H. Al-Bahadly, "Examination of a sensorless rotor-position-measurement method for switched reluctance drive," *IEEE Trans. Ind. Electron.*, vol. 55, no. 1, pp. 288–295, Jan. 2008.

[13] Y. Liang and H. Chen, "Circuit-based flux linkage measurement method with the automated resistance correction for SRM sensorless position control," *IET Electr. Power Appl.*, vol. 12, no. 9, pp. 1396–1406, Nov. 2018.

[14] R. Ortega *et al.*, "Adaptive state observers for sensorless control of switched reluctance motors," *Int. J. Robust Nonlinear Control*, vol. 29, no. 4, pp. 990–1006, Mar. 2019.

[15] A. Khalil, S. Underwood, and I. Husain, "Four-quadrant pulse injection and sliding-mode-observer-based sensorless operation of a switched reluctance machine over entire speed range including zero speed," *IEEE Trans. Ind. Appl*, vol. 43, no. 3, pp. 714–723, May/Jun. 2007.

[16] S. A. Hossain, I. Husain, H. Klode, B. Lequesne, A. M. Omekanda, and S. Gopalakrishnan, "Four-quadrant and zero-speed sensorless control of a switched reluctance motor," *IEEE Trans. Ind. Appl.*, vol. 39, no. 5, pp. 1343–1349, Sep./Oct. 2003.

[17] J.-D. Sun, G.-Z. Cao, S.-D. Huang, Y. Peng, J. He, and Q. Qian, "Sliding-mode-observer-based position estimation for sensorless control of the planar switched reluctance motor," *IEEE Access*, vol. 7, pp. 61034–61045, 2019.

[18] C. A. Hudson, N. S. Lobo, and R. Krishnan, "Sensorless control of single switch-based switched reluctance motor drive using neural network," *IEEE Trans. Ind. Electron.*, vol. 55, no. 1, pp. 321–329, Jan. 2008.

[19] A. D. Cheok and Z. Wang, "Fuzzy logic rotor position estimation based switched reluctance motor DSP drive with accuracy enhancement," *IEEE Trans. Power Electron.*, vol. 20, no. 4, pp. 908–921, Jul. 2005.

[20] S. Paramasivam, S. Vijayan, M. Vasudevan, R. Arumugam, and R. Krishnan, "Real-time verification of AI based rotor position estimation techniques for a 6/4 pole switched reluctance motor drive," *IEEE Trans. Magn.*, vol. 43, no. 7, pp. 3209–3222, Jul. 2007.

[21] H.-Y. Yang, J.-G. Kim, Y.-C. Lim, S.-K. Jeong, and Y.-G. Jung, "Position detection and drive of a toroidal switched reluctance motor (TSRM) using search coils," *IEE Proc. Electr. Power Appl.*, vol. 151, no. 4, pp. 377–384, Jul. 2004.

[22] J. Cai, Z. Liu, Y. Zeng, H. Jia, and Z. Deng, "A hybrid-harmonic-filter-based position estimation method for an SRM with embedded inductive sensing coils," *IEEE Trans. Power Electron.*, vol. 33, no. 12, pp. 10602–10610, Dec. 2018.

[23] L. Shen, J. Wu, and S. Yang, "Initial position estimation in SRM using bootstrap circuit without predefined inductance parameters," *IEEE Trans. Power Electron.*, vol. 26, no. 9, pp. 2449–2456, Sep. 2011.

[24] J. Cai and Z. Deng, "Sensorless control of switched reluctance motor based on phase inductance vectors," *IEEE Trans. Power Electron.*, vol. 27, no. 7, pp. 3410–3423, Jul. 2012.

[25] J.-F. Pan, F.-J. Meng, and N. C. Cheung, "Core loss analysis for the planar switched reluctance motor," *IEEE Trans. Magn.*, vol. 50, no. 2, pp. 813–816, Feb. 2014.

[26] Q.-L. Wang *et al.*, "Position estimation of linear switched reluctance machine with iron losses based on eddy-current effect," *IET Electr. Power Appl.*, vol. 10, no. 8, pp. 772–778, Sep. 2016.

[27] X. Sun, Y. Shen, S. Wang, G. Lei, Z. Yang, and S. Han, "Core losses analysis of a novel 16/10 segmented rotor switched reluctance BSG motor for HEVs using nonlinear lumped parameter equivalent circuit model," *IEEE/ASME Trans. Mechatron.*, vol. 23, no. 2, pp. 747–757, Apr. 2018.

[28] F. J. Perez-Cebolla, A. Martinez-Iturbe, B. Martín-del-Brío, C. Bernal, and A. Bono-Nuez, "Nonlinear lumped-circuit model for switched reluctance motors exhibiting core losses," *IEEE Trans. Ind. Electron.*, vol. 63, no. 6, pp. 3433–3445, Jun. 2016.

[29] H. Cheng, H. Chen, S. Xu, and S. Yang, "Four-quadrant sensorless control in switched reluctance machine drive using pulse injection based on special flux linkage curves," *IET Electr. Power Appl.*, vol. 11, no. 9, pp. 1566–1574, Jul. 2017.

[30] G.-Z. Cao, N. Chen, S.-D. Huang, S.-S. Xiao, and J.-B. He, "Nonlinear modeling of the flux linkage in 2-D plane for the planar switched reluctance motor," *IEEE Trans. Magn.*, vol. 54, no. 11, Nov. 2018, Art. no. 8205805.

Nan Chen received the B.Sc. degree in automation and the M.Sc. degree in control theory and control engineering from Shenzhen University, Shenzhen, China, in 2015 and 2019, respectively.

His research interests include the design, modelling, and control of planar switched reluctance motors and control theory and its applications.

Guang-Zhong Cao (M'15–SM'17) received the B.Sc., M.Sc., and Ph.D. degrees in electrical engineering and automation from Xi'an Jiaotong University, Xi'an, China, in 1989, 1992, and 1996, respectively.

He is currently a Professor with the Department of Automation, and the Director of the Shenzhen Key Laboratory of Electromagnetic Control, College of Mechatronics and Control Engineering, Shenzhen University, Shenzhen, China. He has authored more than 100 articles in refereed journals and conference proceedings. His research interests include control theory, motor design and control, robotics, and Internet of Things.

Su-Dan Huang (M'17) received the B.Sc. and M.Sc. degrees in control theory and control engineering from Shenzhen University, Shenzhen, China, in 2009 and 2012, respectively, and the Ph.D. degree in electrical engineering from Southwest Jiaotong University, Chengdu, China, in 2016.

She is currently an Assistant Professor with the Department of Automation, with the Shenzhen Key Laboratory of Electromagnetic Control, College of Mechatronics and Control Engineering, Shenzhen University, China. Her research interests include the design and control of planar switched reluctance motors, magnetic levitation system, and control theory and its applications.

Jun-Di Sun (S'17) received the M.Sc. degree in control theory and control engineering in 2017 from Shenzhen University, Shenzhen, China, where he is currently working toward the joint Ph.D. degrees in electrical engineering with Southwest Jiaotong University, Chengdu, China and the Shenzhen Key Laboratory of Electromagnetic Control.

His research interests include the design and control of planar switched reluctance motors and sensorless control.